Fu *et al. Journal of Nanobiotechnology* (2025) 23:729
https://doi.org/10.1186/s12951-025-03799-9

Journal of Nanobiotechnology

RESEARCH **Open Access**

Simple-synthesis VO_2 nanoparticles as robust nanozymes for synergistic antibacterial therapy and abscess repair

Weicong Fu[1†], Tian Huang[2†], Yi-Xin Wang[3,4], Jing Zhao[2], Jianliang Shen[5,6*] and Qining Yang[1*]

Abstract
Multidrug resistant (MDR) bacterial infections, particularly those involving methicillin-resistant Staphylococcus aureus (MRSA), pose a grave threat to global population health, necessitating novel therapeutic approaches capable of circumventing existing resistance mechanisms. Biomimetic enzymes, which generate bactericidal reactive oxygen species (ROS) by mimicking natural enzyme activity, represent a highly promising solution. This study reports a straightforward one-step synthesis method for vanadium dioxide (VO_2) nanoparticles, which function as potent biomimetic enzymes exhibiting both oxidase-like and peroxidase-like activities. When combined with near-infrared laser irradiation (808 nm, 1 W/cm^2) for photothermal therapy (PTT), these VO_2 nanoparticles not only mediate local hyperthermia with a photothermal conversion rate of up to 36.9%, but also significantly enhance ROS generation through biomimetic catalysis. This achieves potent synergistic effects between photothermal therapy and chemodynamic therapy (CDT). This combined therapy exhibits potent antibacterial activity against suspended methicillin-resistant Staphylococcus aureus (MRSA) and effectively disrupts preformed biofilms. Furthermore, in a subcutaneous abscess mouse model, VO_2-mediated PTT-CDT treatment efficiently eradicated bacteria, alleviated local inflammation, promoted tissue repair and angiogenesis. In summary, this readily synthesised VO_2 nanozyme system offers an efficient and translatable therapeutic strategy for tackling challenging multidrug-resistant bacterial infections.

Keywords Multidrug-resistant (MDR) bacterial infections, Chemodynamic therapy, Photothermal therapy, Nanozymes, Biocompatibility

---

[†] Weicong Fu and Tian Huang contributed equally to this work as first authors.

*Correspondence:
Jianliang Shen
shenjl@wiucas.ac.cn
Qining Yang
jhyangqn@163.com

Full list of author information is available at the end of the article

Graphical Abstract

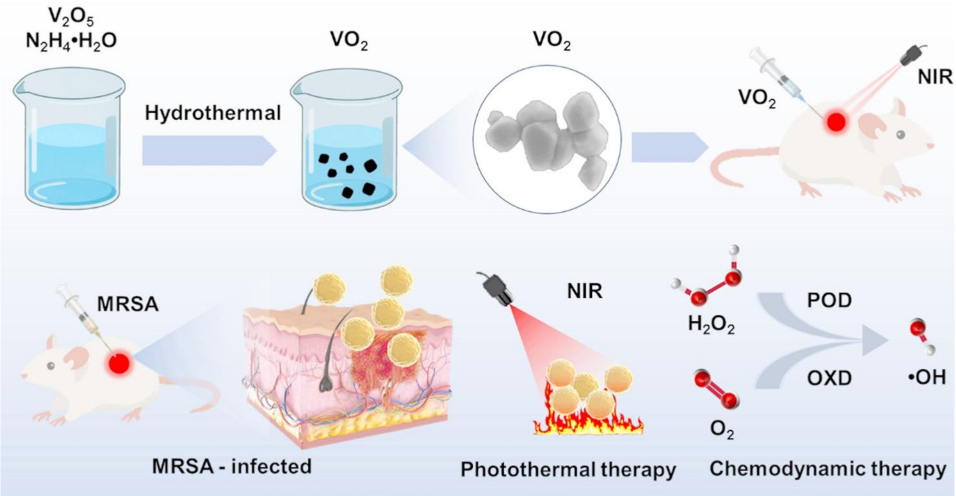

Introduction

The global threat of multidrug-resistant (MDR) bacterial infections poses a critical challenge to modern medicine. According to the World Health Organization (WHO), bacterial antimicrobial resistance (AMR) was directly responsible for an estimated 1.27 million global deaths in 2019 and contributed to an additional 4.95 million deaths, making it a leading cause of mortality worldwide [1]. Without concerted action, this burden is projected to rise dramatically, potentially causing up to 10 million annual deaths by 2050 [2]. *Methicillin-resistant Staphylococcus aureus* (*MRSA*) is a representative multidrug-resistant bacterium that demonstrates resistance to beta-lactam antibiotics due to the presence of the mecA gene [3, 4]. Moreover, *MRSA* also exhibits resistance to other classes of antibiotics, which may be attributed to the presence of additional resistance genes [5, 6]. Consequently, there is an urgent need to develop novel antibacterial strategies. Nanotechnology has emerged as a highly promising platform in this context. Recent breakthroughs in the field of antimicrobial nanomaterials have demonstrated potent antibacterial capabilities through multiple mechanisms. These encompass physical disruption of bacterial membrane structures, photocatalytic generation of reactive oxygen species (ROS), and mimicry of enzymatic activity. Unlike traditional antibiotics, these nanomaterial-based antimicrobials can simultaneously target multiple cellular pathways, making it more difficult for bacteria to develop resistance [7, 8].

Nanozymes have demonstrated significant potential in antibacterial applications in recent years [9]. These nanomaterials possess catalytic activities that are analogous to those of natural enzymes [10, 11]. Nanozymes can replicate the catalytic actions of oxidases [12], peroxidases [13], and other enzymes to generate ROS for antibacterial purposes in CDT [14, 15]. Furthermore, nanozymes can be integrated with other advanced therapeutic modalities, such as photothermal therapy [16], photodynamic therapy [17], and sonodynamic therapy [18], to augment their antibacterial efficacy [19]. Notably, photothermal therapy is capable of converting light energy into heat energy [20], thereby effectively killing bacteria. When employed in combination, certain nanozymes can enhance ROS production under near-infrared irradiation, resulting in remarkable antibacterial potential [21, 22].

Vanadium, a transition metal, has significant potential for applications in chemical engineering, steel production, and energy [23, 24]. In the biomedical sector, vanadium and its compounds have demonstrated the ability to enhance insulin sensitivity and regulate blood glucose levels [25]. Relevant studies indicate that the multifunctional two-dimensional vanadium-based MXene nanoplatform has been utilized as a photothermal transducer for tumor photothermal therapy [26]. Despite extensive research on vanadium and its compounds in anti-tumor and anti-infection applications [27, 28], investigations primarily focus on single-enzyme catalysis or synergistic actions with other materials [29].

Vanadium oxides have found widespread application in various fields, including catalysis and bioimaging applications. However, the potential of VO_2 as a biomedical material is of particular note, due to its photo-thermal conversion properties and inherent catalytic properties [30]. A plethora of synthesis methods for VO_2 have been developed, including sol-gel [31], hydrothermal [32], chemical precipitation [33], and pyrolysis techniques [34]. However, traditional synthesis methods are often complex and difficult to precisely control the crystal phase and particle size of VO_2. Typically, the VO_2 (M) phase obtained by conventional methods necessitates annealing and heating processes to transform the metastable VO_2 (B) phase into the VO_2 (M) phase. This approach poses challenges in achieving both optimal antibacterial efficacy and a straightforward synthetic route simultaneously.

Based on this research, we have developed a vanadium oxide that is easy to synthesize and possesses strong antibacterial properties. The one-step hydrothermal method was employed to synthesize VO_2 (M) without the need for annealing treatment, marking a significant improvement. By introducing hydrazine into the vanadium pentoxide system, hydrazine acts as both a reducing agent and a coordinating ligand to promote the conversion of high vanadium oxidation states to low vanadium oxides [35, 36]. VO_2(M) represents the preponderant form of VO_2, far exceeding the metastable VO_2 (B). This material exhibits excellent photoconversion efficiency (PCE) upon near-infrared stimulation, with this conversion efficiency also possessing the potential to promote reactive oxygen species generation. Moreover, VO_2 demonstrates outstanding antibacterial properties due to its exceptional peroxidase and oxidase activities. Notably, VO_2 has yielded encouraging results in both in vitro and in vivo experiments, indicating its significant potential in combating multidrug-resistant bacterial infections (Fig. 1).

Materials and methods

Materials

Hydrochloric acid and hydrazine hydrate at different concentrations (purities of 80% and 36%, respectively) were purchased from Chengdu Kelong Chemical Co., Ltd. O-Phenylenediamine (OPD), 3,3',5,5'-Tetramethylbenzidine (TMB), and vanadium pentoxide (V_2O_5) with 99% purity were all sourced from Aladdin. Reagents purchased from Solabio included Gram staining kits, Martens trichrome staining kits, tryptic soy broth (TSB) medium, agar, and hematoxylin and eosin (H&E) staining kits. Antibodies (including anti-Arg 1, iNOS, and CD31 antibodies) and the LIVE-DEADTM BacLight TM Bacterial Viability Kit were purchased from Affinity and Invitrogen, respectively.

Measurements

The morphology of VO_2 nanomaterials was primarily observed using transmission electron microscopy (TEM) (FEI Talos F200S G2, Thermo Fisher Scientific), with TEM also employed to acquire diffraction images of the nanomaterials. Concurrently, field emission scanning electron microscopy (SEM) (SU8010, Hitachi) was employed to examine the morphology of MRSA (methicillin-resistant Staphylococcus aureus), while laser confocal microscopy (CLSM) (A1, Nikon) was utilized to observe the fluorescence of VO_2 against MRSA and its anti-biofilm properties.

Synthesis of VO_2

0.45 g of vanadium pentoxide (V_2O_5) was added to 40 mL of deionized (DI) water in a 100 mL beaker. The mixture underwent 30 min of ultrasonic treatment in an ultrasonic cleaner (Ningbo Scientz Biotechnology Co., Ltd, SB-5200DT). Throughout the ultrasonication process, the beaker was placed in an ice-water bath to prevent overheating, ultimately yielding a deep yellow, uniformly dispersed solution. A separate potassium hydroxide aqueous solution was prepared by dissolving 0.42 g of potassium hydroxide in 10 mL of deionized water. Subsequently, this KOH solution was added dropwise (approximately one drop per second) to the V_2O_5

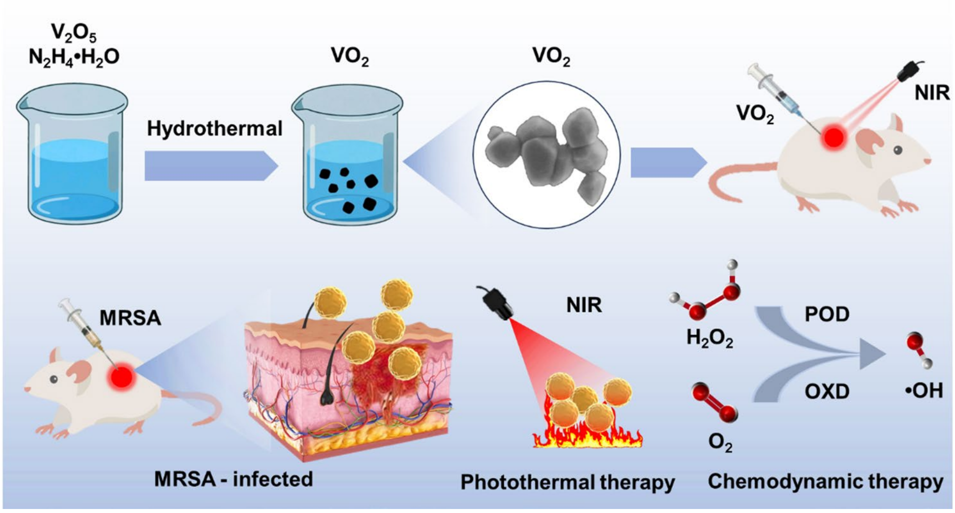

Fig. 1 The description of the synthesis procedure of VO_2 and the efficacy of VO_2 in laser irradiation against *MRSA*-infected abscesses in vivo

dispersion under vigorous magnetic stirring at 500 rpm. After complete addition, stirring continued at 500 rpm for exactly 10 min at room temperature (25 ± 2 °C). The mixture turned pure yellow, indicating the formation of soluble vanadate. The beaker was then transferred to and maintained in an ice-water bath (0–4 °C).A diluted hydrazine hydrate solution (25%) was prepared by diluting the commercial stock (80%) with DI water.0.51 mL of this 25% hydrazine hydrate solution was added dropwise (approximately 1 drop every 2–3 s) into the cold, stirred reaction mixture. The color of the reaction mixture was observed to turn from yellow to green, and then to a dark brown during this step. The pH of the resulting dark brown reaction mixture was carefully adjusted to 3.3–3.5 using hydrochloric acid (HCl, 36.0%–38.0%) added dropwise under stirring.After pH adjustment, the mixture was stirred for an additional 2 h at room temperature.The final black solution was transferred into a 100 mL polytetrafluoroethylene (PTFE)-lined stainless steel autoclave, filling approximately 80% of its volume. The autoclave was sealed and placed in a preheated oven at 200 °C for 24 h. After natural cooling to room temperature, the black precipitate was collected by centrifugation at 10,000 rpm for 10 min and washed five times with deionized (DI) water to remove any ionic by-products. The final product was dried in a vacuum oven at 60 °C for 12 h before further characterization and use.

Photothermal performance of VO_2

The photothermal properties of VO_2 nanoparticles were systematically evaluated. First, their ultraviolet-visible-near-infrared absorption spectra were measured using a UV-vis-NIR spectrophotometer (CARY5000, Agilent), confirming their strong near-infrared absorption characteristics. Subsequently, the photothermal heating curves were measured. A total of 1 mL of each VO_2 dispersion at the aforementioned concentrations was placed in a quartz cuvette. Subsequently, the sample was irradiated using an 808 nm near-infrared (NIR) laser diode (MDL-III-808). The laser beam was adjusted to form an irradiation spot of approximately 1 cm^2 on the liquid surface, achieving a power density of 1 W/cm^2. This parameter was calibrated using a laser power meter (S425C, Thorlabs). The temperature change of the solution was monitored and recorded every 10 s for 8 min using a digital thermometer with a K-type thermocouple probe inserted directly into the solution, coupled with a real-time infrared thermal imaging camera (FLIR E6, Teledyne FLIR LLC) to visualize the temperature distribution. To examine the effects of concentration and power on the photothermal performance of VO_2, we subjected VO_2 samples at different consistencies to continuous irradiation under near-infrared radiation at power levels of 0.5 and 1.0 W cm^{-2} for 8 min. Thermal stability was evaluated through five cycles of cooling and heating processes (100 μg mL^{-1}, 1.0 W cm^{-2}). Temperature changes were monitored using an infrared thermal imager, and the photothermal conversion efficiency was calculated based on relevant literature [37].

Capacity to generate ROS of VO_2

The detection of reactive oxygen species primarily employs 3,3',5,5'-tetramethylbenzidine (TMB), o-phenylenediamine (OPD), and 5,5-dimethyl-1-pyrrolidone N-oxide (DMPO). To investigate the effect of different pH values on VO_2 catalytic performance, phosphate buffer solutions (0.1 M) with pH values of 4.0, 5.0, 6.0, 7.0, and 8.0 were prepared using sodium dihydrogen phosphate and sodium hydrogen phosphate.The pH of each buffer was precisely calibrated using a calibrated digital pH meter. In a standard reaction, 500 μL of phosphate buffer at a specific pH was mixed with 50 μL of VO_2 dispersion (final concentration: 100 μg/mL) and 50 μL of TMB solution (10 mM in DMSO, final concentration: 1 mM) in a 1.5 mL microcentrifuge tube. For peroxidase-like activity assessment, 50 μL of H_2O_2 (30 wt%, diluted to a final concentration of 100 μM) was added to the mixture.The reaction mixture was vortexed for 10 s and then incubated at room temperature for 10 min. After incubation, 200 μL of the reaction solution was immediately transferred to a 96-well plate. The absorbance at 652 nm was measured using a microplate reader (BioTek Synergy H1). All experiments were performed in triplicate. Additionally, we investigated the time-dependent kinetics of VO_2 enzyme activity. We prepared a mixture containing 100 μL phosphate buffer (0.1 M, pH 5.0), 100 μL VO_2 (final concentration: 100 μg/mL), and 100 μL OPD solution (prepared in deionized water at pH 5.0), 100 μL VO_2 (final concentration: 100 μg/mL), and 100 μL OPD solution (prepared in deionized water at 10 mM, final concentration 1 mM). Immediately after mixing, 1 mL of the mixture was transferred to a quartz cuvette. Ultraviolet absorption spectra were measured at different time points (total duration of 5 min, with measurements taken at one-minute intervals) were determined using a UV-visible-near-infrared spectrophotometer (UV-vis-NIR) (CARY5000, Agilent). Subsequently, the procedure was repeated while varying the final VO_2 concentration (0, 20, 40, 60, 80, and 100 μg/mL). UV absorption spectra were measured at a fixed reaction time (5 min) to evaluate the concentration-dependent kinetics of VO_2.

Antibacterial properties by VO_2 mediated PTT + CDT

The antibacterial efficacy of VO_2 nanoparticles against Methicillin-resistant Staphylococcus aureus (MRSA, ATCC 43300) was evaluated in vitro through colony counting, scanning electron microscopy (SEM), and

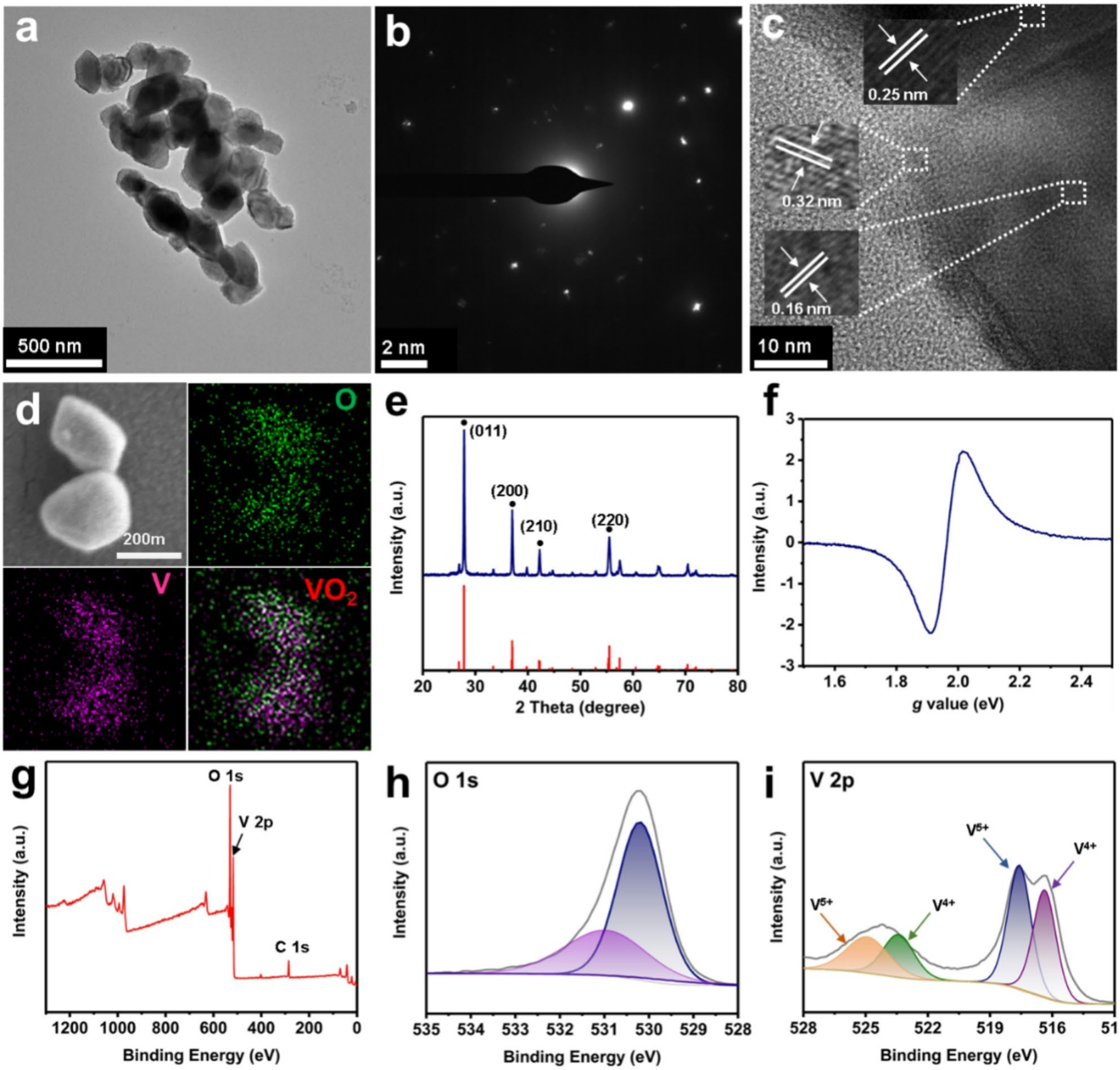

Fig. 2 Characterization of VO_2. (**a**) TEM image and (**b**) SAED pattern of VO_2. Scale bar, 500 nm, 2 nm. (**c**) HRTEM image of VO_2. Scale bar, 10 nm. (**d**) Element mapping for vanadium (V) and oxygen (O) of VO_2. Scale bar, 200 nm. (**e**) XRD of VO_2 with inserted references. (**f**) EPR spectra of VO_2. (**g**) XPS survey spectra and High-resolution XPS spectra of (**h**) O 1 s region and (**i**) V 2p region of VO_2

confocal laser scanning microscopy (CLSM). The detailed steps are as follows:

Bacterial Culture: A single colony of MRSA was inoculated into 10 mL of Tryptic Soy Broth (TSB) and cultured overnight at 37 °C with shaking at 200 rpm to reach the mid-logarithmic phase. The bacterial cells were harvested by centrifugation at 5000 rpm for 5 min, washed twice with phosphate-buffered saline (PBS, 0.01 M, pH 7.4), and resuspended in PBS. The bacterial concentration was adjusted to 1×10^8 CFU/mL (OD600 = 0.1) using a microplate reader for subsequent experiments.

Experimental Procedure: Initially, we evaluated the antibacterial activity of VO_2 using agar plates. Bacterial suspensions were divided into five treatment groups ($n = 3$ per group): PBS (control), VO_2 (100 μg/mL), VO_2 + H_2O_2 (100 μg/mL VO_2 + 100 μM H_2O_2),, VO_2 + near-infrared (NIR) (100 μg/mL VO_2 + NIR irradiation), and VO_2 + H_2O_2 + NIR (100 μg/mL VO_2 + 100 μM H_2O_2 + NIR irradiation). For each group, 100 μL bacterial suspension was mixed with 100 μL corresponding treatment solution in a 1.5 mL centrifuge tube. The near-infrared irradiation group received 808 nm laser irradiation (1 W/cm², 10 min), with temperature changes monitored

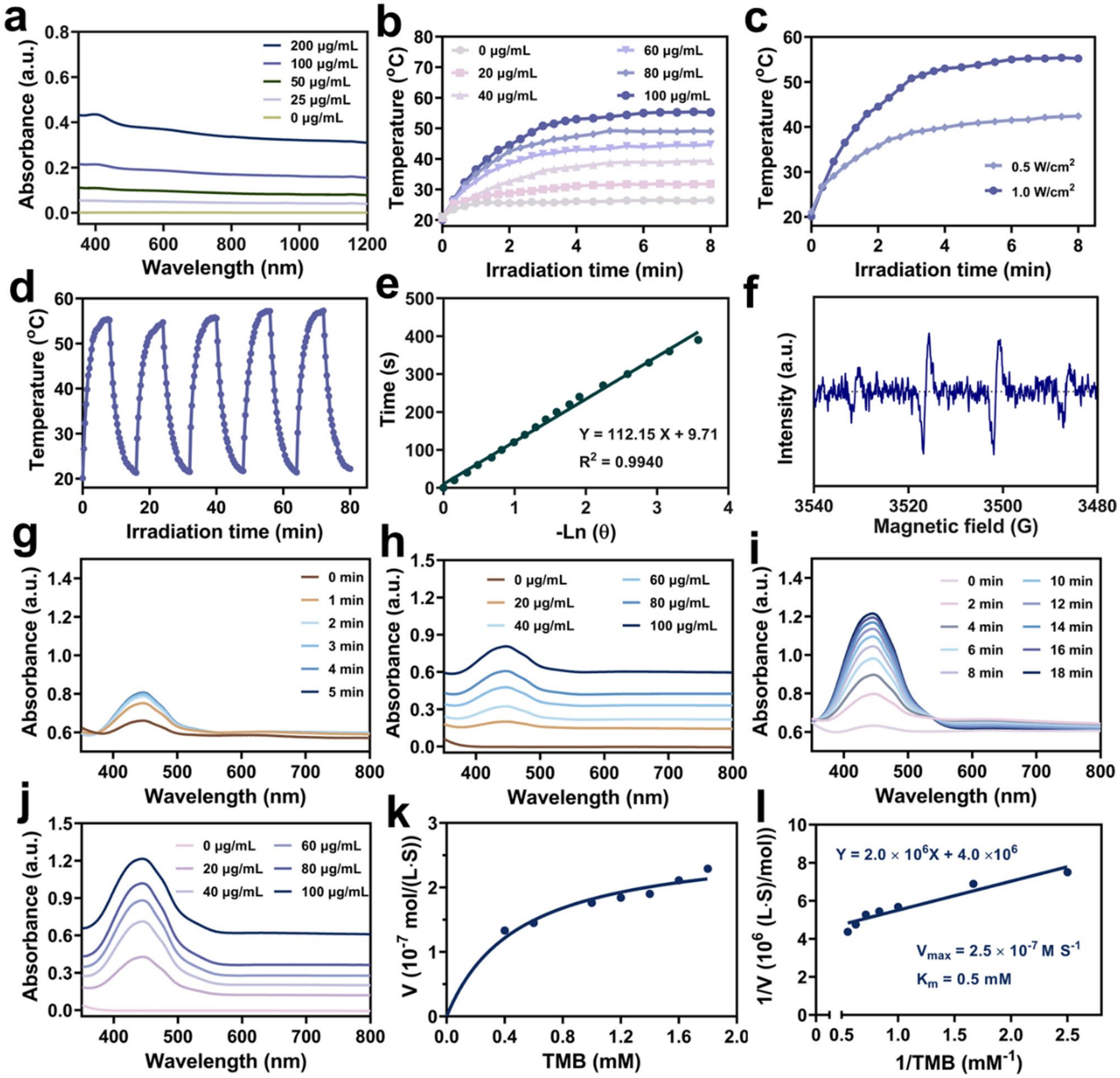

Fig. 3 The photothermal properties and reactive oxygen species (ROS) generation capabilities of VO_2 were investigated. (a) The UV-vis-NIR absorption spectra of VO_2 at various concentrations. (**b**) The photothermal curves of VO_2 at different concentrations under 808 nm laser irradiation for a duration of 8 min. (**c**) The temperature variations of VO_2 under varying laser power levels. (**d**) The thermal stability of VO_2 was assessed over five hot and cold cycles. (**e**) Linear fit plot of time and –Ln (θ) from cooling time. (**f**) ESR spectra of DMPO/•OH adducts in VO_2 (**g**, **h**) uses OPD as the substrate, the UV absorption spectra of VO_2 at various times and concentrations. In (**I**, **j**), OPD is again employed as the substrate, the UV absorption spectra of VO_2 at various times and concentrations after adding H_2O_2. (**k**) Michaelis-Menten kinetic analysis for VO_2 with TMB as substrates. (**l**) Lineweaver-Burk fitting for VO_2 with TMB as substrates

throughout. The VO_2 + H_2O_2 group was incubated in the dark for 10 min. After treatment, 100 μL samples from each tube were serially diluted 10^5 times with PBS. 100 μL of each dilution was evenly spread onto TSB agar plates. Plates were incubated at 37 °C for 24 h, after which colonies were counted and results expressed as CFU/mL.

Subsequently, we placed MRSA suspensions (1 mL, approximately 10^8 CFU/mL) from each treatment group into 2 mL centrifuge tubes using the aforementioned method. After treatment, bacteria were collected by centrifugation (8000 rpm, 5 min) and fixed overnight at 4 °C with 2.5% glutaraldehyde in PBS. Dehydrate the fixed cells using a graded ethanol series (10%, 30%, 50%, 70%, 90%, and 100% ethanol, 10 min each). Deposit 10 μL of the dehydrated bacterial suspension onto a clean silicon wafer. After air-drying, coat with a 2 nm thick platinum layer using a magnetron sputtering coating machine. Bacterial morphology was ultimately observed using a field emission scanning electron microscope (SU8010, Hitachi) at an acceleration voltage of 5 kV.

After treatment, 100 μL of the bacterial suspension was incubated with 2 μL of the Live/Dead BacLight Bacterial Viability Kit in the dark for 15 min at room temperature. 10 μL of the stained suspension was then placed on a glass slide, covered with a coverslip, and immediately observed under a confocal laser scanning microscope (A1, NIKON). SYTO9 (green fluorescence, excitation/emission: 480/500 nm) and PI (red fluorescence, excitation/emission: 490/635 nm) were used to label live and dead bacteria, respectively.

Biofilm disruption by VO_2-mediated PTT + CDT

To investigate the eradication and inhibition effects of VO_2 on biofilms, we employed both crystal violet staining and confocal laser scanning microscopy (CLSM).

Biofilm Inhibition Assay: MRSA was diluted to 1×10^7 CFU/mL in fresh TSB medium. 1 mL of this suspension was added to each well of a 24-well cell culture plate and incubated at 37 °C for 24 h to allow biofilm formation. After incubation, the planktonic bacteria and medium were gently aspirated, and the formed biofilms were washed twice with PBS. Then, 1 mL of the different treatment solutions (same groups as in Sect. "Antibacterial properties by VO2 mediated PTT + CDT") in fresh TSB was added to the respective wells. The plate was incubated for another 4 h. For NIR groups, the entire plate was irradiated with the 808 nm laser at 1 W/cm^2 for 10 min prior to staining.

Biofilm Eradication Assay: Biofilms were formed as described above. After 24 h, instead of fresh medium with treatments, the pre-formed biofilms were directly treated with the different solutions (in PBS) and subjected to NIR irradiation as applicable. This model tests the ability to disrupt mature biofilms.

After the respective treatments, the biofilms were washed gently with PBS and air-dried for 30 min. Then, 1 mL of 1% (w/v) crystal violet solution was added to each well and stained for 1 h at room temperature. The unbound dye was removed, and the wells were gently rinsed with PBS. The bound crystal violet was solubilized by adding 1 mL of 33% (v/v) acetic acid to each well for 30 min with gentle shaking. 200 μL of the solution from each well was transferred to a 96-well plate, and the absorbance was measured at 590 nm using a microplate reader.Biofilms were grown and treated on sterile glass coverslips placed inside the 24-well plate. After treatment, the biofilms on the coverslips were stained using the SYTO9/PI mixture as described in Sect. "Antibacterial properties by VO2 mediated PTT + CDT" for 15 min in the dark. The coverslips were then carefully removed, inverted onto glass slides, and visualized under the CLSM.

Biosafety assessment of VO_2

The hemolytic potential of SHF1 hydrogel was evaluated in vitro using red blood cells derived from rats. Erythrocytes were isolated by centrifuging freshly collected rat blood containing 2% ascorbic acid for 10 min, followed by triple washing with PBS. A volume of 1 mL of the resulting cell suspension was transferred into individual tubes. Each tube then received 100 mg of hydrogel. For comparison, 100 mg of 0.1% Triton X-100 and PBS were included as positive and negative benchmarks, respectively. After a 3-hour incubation at 37 °C, samples underwent centrifugation at 2500 rpm for 5 min. Supernatant absorbance at 545 nm was measured using a UV–VIS–NIR device. The percentage of hemolysis was determined by the following formula: Hemolysis (%) = $[(A_h - A_p)/(A_t - A_p)] \times 100\%$, where A_t, A_p, and A_h correspond to absorbance values for Triton, PBS, and hydrogel treatments, respectively. Erythrocytes exposed to Triton and PBS functioned as positive and negative controls.

The biocompatibility of VO_2 nanoparticles was initially assessed through a hemolysis assay. Freshly collected mouse blood containing 2% ascorbic acid was centrifuged for 10 min, followed by three washes with PBS to isolate red blood cells. Subsequently, VO_2 samples at different concentrations (0, 50, 100, 150, 200, 250, and 300 μg/mL) were mixed with the erythrocytes, with water serving as the positive control and PBS as the negative control. The absorbance of the supernatant at 540 nm was measured using a UV-Vis-NIR spectrophotometer. The haemolysis rate was calculated as: $[(Ah - Ai)/(At - Ai)] \times 100\%$, where At, Ai, and Ah represent the absorbance values of double-distilled water (DDW), PBS, and the hydrogel supernatant, respectively [38, 39]. Following subcutaneous injection of PBS and VO_2, blood samples were collected from mice 24 h later for analytical assessment. Furthermore, to evaluate the long-term biocompatibility of VO_2, hearts, livers, spleens, lungs, and kidneys were harvested from mice 10 days post-injection for haematoxylin and eosin staining.

In vivo antibacterial evaluation of VO_2-mediated PTT + CDT

All procedures involving animals were performed in accordance with the protocol approved by the Wenzhou Institute, University of Chinese Academy of Sciences (Wenzhou Institute of Biomaterials & Engineering) (WIUCAS24072204).Female BALB/c mice (6–8 weeks old) were anesthetized, and the dorsal hair was shaved. On day −1, a subcutaneous abscess was induced by injecting 80 μL of MRSA suspension (2×10^7 CFU/mL) into the shaved area. On day 0, when the abscess was formed, the mice were randomly divided into five groups

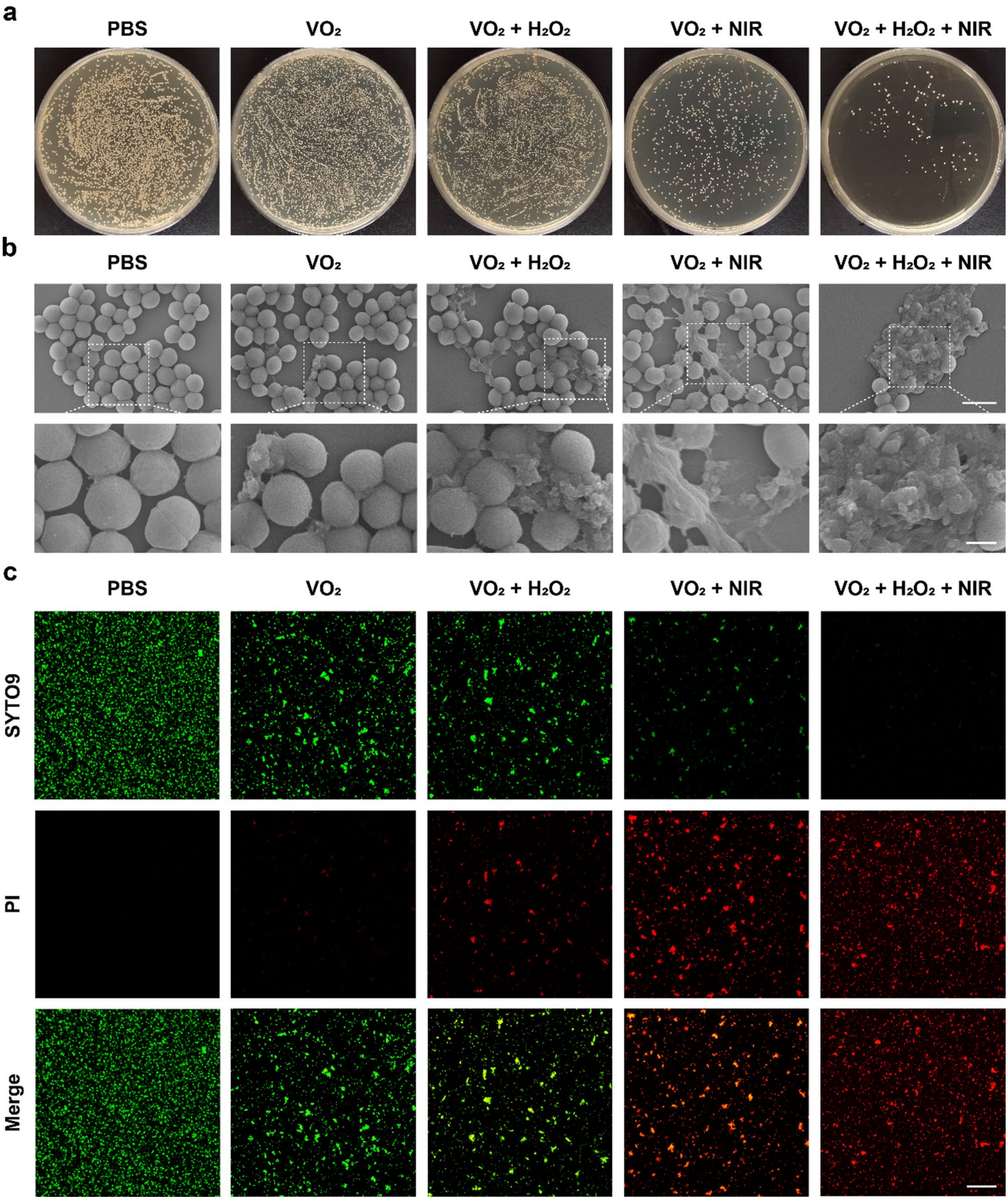

Fig. 4 The antibacterial effect of VO_2 nanoparticles on *MRSA* was assessed in vitro. (**a**) The growth of *MRSA* in bacterial culture dishes was observed after incubation at 37 °C for 12 h. (**b**) SEM images were obtained to analyze bacterial morphology following various treatments. Scale bar, 1.5 μm, 0.5 μm. (**c**) CLSM images were utilized for the live/dead assay *MRSA* after different treatments. Scale bar, 100 μm

($n = 3$ per group), corresponding to the in vitro treatment groups. For treatment, 40 μL of the respective solutions (PBS or VO_2 with/without H_2O_2) was injected locally into the abscess. The NIR irradiation groups were exposed to an 808 nm laser at 1 W/cm^2 for 10 min immediately after injection. The temperature change at the abscess site was monitored using an IR thermal camera.The abscess size and mouse body weight were recorded every other day for 10 days. The abscess area was calculated from photographic images using ImageJ software. On day 10, the mice were euthanized. The skin tissue from the abscess was excised, homogenized in 1 mL of PBS, serially diluted, and plated on TSB agar plates for bacterial counting. The excised skin tissues were also fixed for subsequent histological and immunofluorescence staining.

Statistical analysis

Three blinded investigators independently assessed macroscopic and histological findings. Results were displayed as mean ± SD, generated via GraphPad Prism 8 software. Statistical analysis utilized either the unpaired Student's t-test or the Mann-Whitney U test, chosen according to data distribution patterns, to evaluate significance. All experimental replicates were of biological origin. The following thresholds were used to denote statistical relevance: NS ($P > 0.05$), $^{*}P \leq 0.05$, $^{**}P \leq 0.01$, $^{***}P \leq 0.001$, $^{****}P \leq 0.0001$.

Results and discussion

Synthesis and physicochemical characterization of vanadium dioxide

VO_2 nanoparticles containing abundant oxygen vacancies were synthesized via the hydrothermal method. Following synthesis, we evaluated the morphology of VO_2. Transmission electron microscopy (TEM) results revealed that VO_2 nanoparticles predominantly exhibited spherical or polyhedral shapes, with a diameter of approximately 160 nm (Fig. 2a and S1). However, the hydrated particle size of VO_2 nanoparticles measured by dynamic light scattering was approximately 250 nm, slightly larger than the dry particle size observed by transmission electron microscopy (approximately 154 nm). This discrepancy stems from the hydration layer on the particle surface. The zero potential value of −15.9 mV indicates a moderately negative charge on the particle surface, which contributes to its electrostatic stability in aqueous solution, preventing rapid precipitation and further aggregation (Figure S2). Bright diffraction spots in the electron diffraction pattern reveal that VO_2 nanoparticles exhibit interplanar spacings of 0.32 nm, 0.16 nm, and 0.25 nm (corresponding to the 011, 220, and 200 crystal planes, respectively) (Fig. 2c). Furthermore, elemental analysis of the VO_2 nanoparticles via scanning electron microscopy (SEM) revealed the presence of vanadium (V) and oxygen (O) elements, with uniform distribution of these elements throughout the nanoparticles (Fig. 2d). Furthermore, the X-ray diffraction (XRD) pattern revealed characteristic peaks of the synthesized VO_2 matching the VO_2 standard PDF card (PDF#82–0661) (Fig. 2e). Additionally, electron paramagnetic resonance (EPR) detection yielded a characteristic signal at $g = 1.96$, typically associated with oxygen vacancies arising from surface defects in the sample (Fig. 2f). Energy-dispersive X-ray spectroscopy (EDS) line scans and elemental mapping along the arrow direction on a single nanoparticle validated the elemental analysis (Figure S3). X-ray photoelectron spectroscopy (XPS) analysis further confirmed the presence of oxygen and vanadium elements (Fig. 2g). High-resolution XPS V 2p spectra reveal two dominant peaks in VO_2: 517.4 eV corresponding to V^{5+} and 516.4 eV to V^{4+} (Fig. 2h). The O 1s level was resolved into two components: a 530.9 eV peak attributed to the oxygen lattice and a 531.8 eV peak associated with oxygen vacancies (Fig. 2i). Collectively, these results demonstrate the successful synthesis of VO_2 nanoparticles.

Photothermal performance of VO_2

To investigate the photothermal properties of VO_2, we studied its ultraviolet absorption characteristics using ultraviolet-visible-near-infrared spectroscopy. The spectrum of the VO_2 dispersion (Fig. 3a) exhibits broadband absorption across wavelengths ranging from 350 to 1200 nm. This broad absorption range is characteristic of VO_2 (M) nanoparticles and forms the basis for their photothermal performance. Absorption in the near-infrared region (particularly near 808 nm) is crucial for VO_2's role as a photothermal agent under near-infrared laser irradiation. Therefore, we further investigated the photothermal properties of VO_2 nanoparticles in this region by irradiating them with near-infrared radiation (808 nm, 1 W/cm^2). Results from Fig. 3b demonstrate that VO_2 functions as an efficient photosensitizer, primarily evidenced by the increase in VO_2 temperature with rising concentration. At 100 μg/mL, the VO_2 solution reached 53.8 °C within just 5 min—a photothermal response significantly superior to that of aqueous solutions irradiated for the same duration (only 26.1 °C within 5 min). Additionally, the temperature of the VO_2 nanoparticle dispersion varies with irradiation power. Under 0.5 W near-infrared irradiation, the dispersion reached 42.4 °C after 8 min, whereas 1 W irradiation elevated it to 55.2 °C (Fig. 3c). Furthermore, real-time thermal imaging monitoring using an infrared camera confirmed the significant photothermal effect of the VO_2 dispersion (Figure S4b). Moreover, a cyclic test involving five cycles of near-infrared irradiation (808 nm, 1 W/cm^2) demonstrated no significant temperature fluctuations in the VO_2 dispersion under alternating heating and cooling conditions,

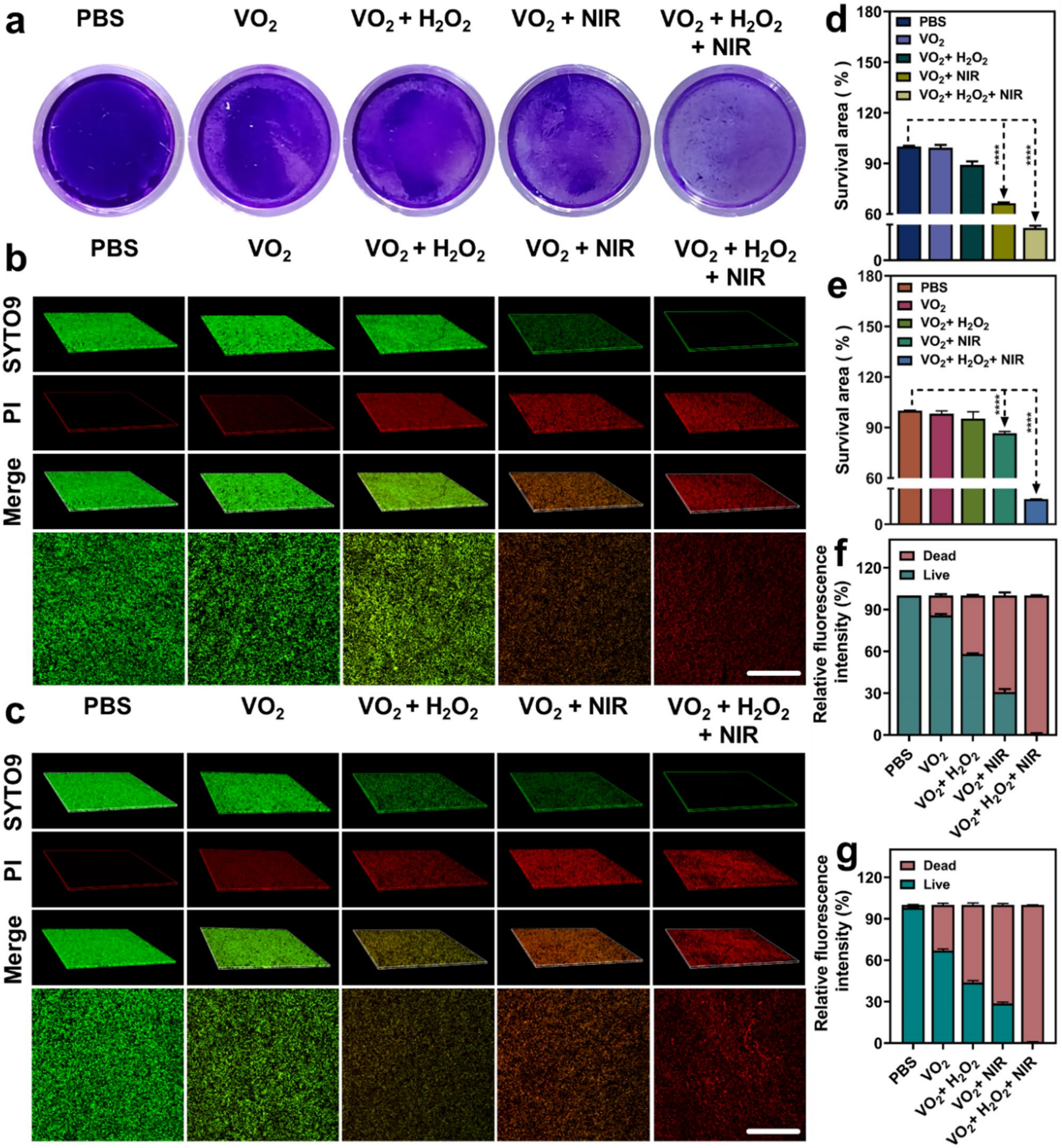

Fig. 5 The antibiofilm effects of VO_2 nanoparticles were assessed through various experimental approaches. (**a**) Typical images of crystal violet staining are presented for each group following treatment aimed at inhibiting *MRSA* biofilm formation. (**b**) CLSM image illustrates the biofilm stained with SYTO9/PI after the inhibition treatment. Scale bar, 200 µm. (**c**) CLSM image depicts the biofilm stained with SYTO9/PI following the eradication treatment. Scale bar, 200 µm. (**d**) Quantitative data on biofilm biomass were obtained from (**a**). (**e**) Quantitative data of crystal violet-stained biomass after the biofilm eradication treatment are presented. (**f**) Quantitative data on biofilm biomass derived from (**b**) are included. (**g**) The quantitative data on biofilm biomass were obtained from (**c**). Data are presented as mean ± SD ($n = 3$), $^{*}p < 0.05$, $^{**}p < 0.01$, $^{***}p < 0.001$, $^{****}p < 0.0001$

highlighting the excellent photothermal stability of VO_2 nanoparticles (Fig. 3d). Subsequently, based on the thermal cycling results and the ultraviolet absorption characteristics of the VO_2 nanoparticle dispersion, we calculated a photoconversion efficiency of 36.9% (Fig. 3e and S2a). This demonstrates the remarkable efficacy of VO_2 in converting light energy into thermal energy.

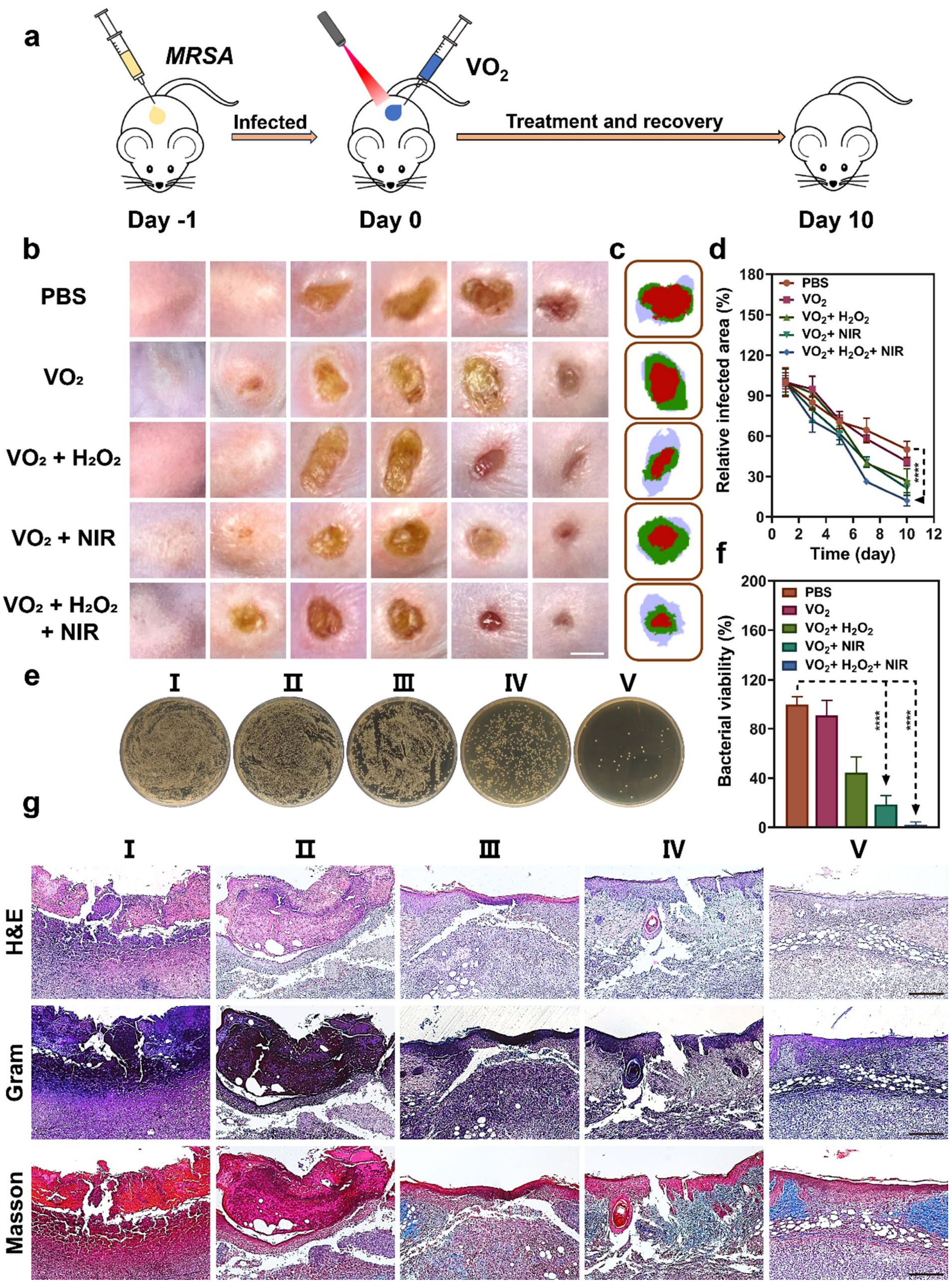

Fig. 6 (See legend on next page.)

(See figure on previous page.)

Fig. 6 Anti-infectious treatment of subcutaneous abscesses in mice with VO_2 nanoparticles. (**a**) Schematic diagram of establishing mice subcutaneous abscess model. (**b**) Representative images of abscesses on days 0, 1, 3, 5, 7, and 10. Scale bar, 5 mm. (**c**) Plot of abscess area over time. (**d**) Statistical analysis of abscess area. (**e**) Pictures of bacteria in abscess tissue of different treatment groups on the tenth day. (**f**) Analysis of bacterial population data derived from (**e**). (**g**) H&E, Gram and Masson staining of abscess skin tissue after different treatments. Scale bar, 100 μm. Ⅰ: PBS; Ⅱ: VO_2; Ⅲ: $VO_2+H_2O_2$; Ⅳ: VO_2+NIR; Ⅴ: $VO_2+H_2O_2+NIR$. Data are presented as mean ± SD ($n=3$), $*p<0.05$, $**p<0.01$, $***p<0.001$, $****p<0.0001$

Capacity to generate ROS of VO_2

We initially evaluated the enzymatic activity of VO_2 under different pH conditions, including oxidase and peroxidase activities. For this purpose, we selected OPD and TMB as substrates and employed colorimetric assays. In the presence of VO_2, colorless TMB is oxidized into a blue-green product, enabling quantification of ROS production via absorbance at a specific wavelength (652 nm) [40]. As shown in Figure S5, VO_2 exhibited robust enzymatic activity under acidic conditions, which diminished with increasing pH—a phenomenon particularly pronounced in peroxidase activity. Studies indicate that bacterial infections generate lactic acid metabolites, while immune cells release acidic metabolites during stress responses, leading to decreased pH at infection sites. To simulate the microenvironment at infection sites, we evaluated enzyme activity under pH 5.0 conditions [41]. OPD is a commonly used hydroxyl radical scavenger; in the presence of hydroxyl radicals, OPD generates a yellow product. Quantification of ROS production is achieved by measuring absorbance at 440 nm. Therefore, we employed OPD as a substrate to investigate ROS generation by VO_2 at different time points and concentrations [42]. As illustrated in Fig. 3g, the reaction was essentially complete within 2 min after OPD addition (Fig. 3h), with proportional increases in ROS production at higher concentrations, which demonstrated the excellent oxidase activity of VO_2. The prolongation of reaction time upon H_2O_2 addition enhanced the generation of hydroxyl radicals, while an increase in •OH production was observed across different VO_2 concentrations (Fig. 3i and j). We have also validated the enzymatic activity of VO_2 using TMB as a substrate, with results consistent with the aforementioned experiments (Figure S6).

Additionally, we determined hydroxyl radicals using electron spin resonance (ESR) technology combined with DMPO [43]. The above results suggested that the characteristic strong 1:2:2:1 signal of hydroxyl radicals was respected upon H_2O_2 addition (Fig. 3f). This supported the robust oxidase and peroxidase energies of VO_2. Figure S7 registers the color changes of VO_2 at different concentrations using TMB/OPD as substrates. Subsequently, we quantitatively evaluated the catalytic efficiency of VO_2 through steady-state kinetic analysis [44]. As shown in Fig. 3k and l, the lower Km value and higher Vmax value indicate significantly enhanced affinity between the catalyst and substrate [45]. VO_2 exhibits a low Km value and high Vmax value, indicating robust catalytic performance. Finally, the effects of light and heat on enzyme activity were investigated (Figure S8). The results displayed enhanced reactive oxygen species (ROS) generation under near-infrared irradiation.

Antibacterial properties by VO_2 mediated PTT + CDT

Previous studies have demonstrated that VO_2 nanoparticles not only exhibit excellent photothermal properties but also possess the ability to generate free radicals. These dual potentials enable potent synergistic effects between photothermal therapy and chemo-dynamic therapy. This combined approach of photothermal and chemo-dynamic therapies may exhibit superior antibacterial performance. Therefore, we evaluated the antibacterial efficacy of VO_2 using MRSA bacteria. We first assessed the antibacterial activity of VO_2 using agar plates (Fig. 4a). Results showed MRSA survival rates of 87.29%, 74.28%, and 17.57% after treatment with VO_2, VO_2 + H_2O_2, and VO_2 + NIR, respectively. Under simultaneous near-infrared irradiation and H_2O_2 presence, MRSA survival rate dropped to 5.36% with VO_2 treatment. highlighting VO_2's superior antibacterial performance through synergistic photothermal and chemodynamic effects (Figure S9a). Additionally, SEM analysis revealed morphological changes in MRSA bacteria post-treatment. As shown in Fig. 4b, bacteria in the PBS group exhibited smooth surfaces and intact, rounded shapes. In contrast, bacteria treated with VO_2, VO_2 + H_2O_2, and VO_2 + NIR exhibited varying degrees of wrinkling, with the VO_2 + NIR group showing the most severe wrinkling. MRSA bacteria treated with VO_2 + NIR were visibly ruptured with some leakage of cellular contents. However, bacteria treated with VO_2 + H_2O_2 + NIR showed severely disrupted morphology and extensive cell death. This further indicates that the combined photothermal and chemotherapeutic approach significantly disrupts bacterial membranes.

Furthermore, we employed a live/dead staining kit to assess bacterial survival rates, where green fluorescence indicated viable bacteria and red fluorescence signified dead bacteria. Results showed significant green fluorescence in both the PBS and VO_2 groups, while the VO_2 + H_2O_2 group exhibited only minimal red fluorescence (Fig. 4c). In contrast, the VO_2 + NIR group exhibited markedly reduced green fluorescence, while the VO_2 + H_2O_2 + NIR group showed significantly enhanced red fluorescence. Quantitative fluorescence analysis further revealed that the proportion of red fluorescence increased to 96.16% compared to the PBS group (Figure S9b). These findings further confirm that VO_2 demonstrates outstanding antibacterial efficacy when combined with PTT and CDT.

Biofilm disruption by VO_2-mediated PTT + CDT

Biofilms are a significant factor that contribute to the difficulty in eradicating multidrug-resistant (MDR) bacteria, as their presence substantially diminishes the bactericidal effects of antimicrobial agents. Existing research indicates that bacterial biofilms impede the efficacy of antibiotics and the immune system. Photothermal therapy exhibits dual effects of inhibiting and eliminating biofilms; however, the effectiveness of photothermal therapy alone is limited. Therefore, a combination of multiple approaches is necessary for eradicating MDR bacteria [46, 47]. VO_2 exhibits outstanding oxidase and peroxidase activities, generating substantial reactive oxygen species (ROS) that effectively disrupt bacterial biofilms. Therefore, we evaluated the inhibition and eradication effects of VO_2 nanoparticles on biofilms using crystal violet staining and fluorescence staining. Crystal violet staining revealed VO_2's inhibitory effect on biofilm formation, with staining intensity positively correlated with biofilm thickness and structural integrity—darker shades indicating higher density. Figure 5a shows that the VO_2 + H_2O_2 + NIR group exhibited the lightest shade compared to the PBS control group. Quantitative analysis of absorbance at 590 nm further confirmed this observation (Fig. 5d). In addition, we conducted an in-depth investigation of VO_2's inhibitory effect on biofilms using a live/dead cell staining kit. As depicted in Fig. 5b, the VO2 + H2O2 + NIR group exhibited significant red fluorescence while green fluorescence was nearly absent (relative to the PBS group). Quantitative fluorescence analysis revealed that the red fluorescence ratio in this combination group increased to 98.99%, indicating effective inhibition of biofilm formation by VO2 (Fig. 5f). To validate VO2's biofilm clearance efficacy, we supplemented the study with crystal violet staining and live/dead cell staining assays, further confirming VO2's anti-biofilm activity (Fig. 5c, e and g, and Supplementary Figure S10).

Biosafety assessment of VO_2

Excellent biocompatibility is crucial for biomaterials [48]. We first evaluated VO_2's in vitro biocompatibility using a hemolysis assay. Results showed that even at a concentration of 300 μg/mL, VO_2 maintained a low hemolysis rate of only 3.97%, preliminarily indicating its favorable blood compatibility (Figures S13). To further validate VO2's in vivo biocompatibility, we conducted routine blood tests and biochemical analyses, along with toxicological evaluations of mouse tissues (heart, liver, spleen, lungs, and kidneys) (Figures S14, S15). Results showed that routine blood parameters and biochemical indicators remained within normal ranges across all groups, with no significant abnormalities observed. Concurrently, organs from mice treated with VO2 for 10 days showed no significant differences compared to controls, indicating no apparent toxicity. This confirms VO2 exhibits favorable biocompatibility both in vivo and in vitro.

In vivo antibacterial evaluation of VO_2-mediated PTT + CDT

Recognizing VO2's exceptional antibacterial properties demonstrated in vitro, a subcutaneous abscess model in mice was used to further validate its antimicrobial efficacy. The establishment process of this model is illustrated in Fig. 6a: MRSA inoculum was injected subcutaneously into mice on day 1, followed by initiation of drug treatment on day 0. The subcutaneous abscess recovery was continuously monitored for ten days. As illustrated in Fig. 6b, all five of the groups successfully established abscess models by Day 0. The abscesses ruptured and began healing by Day 3. By day 10, the infected wound area in the VO_2 + H_2O_2 + near-infrared light group decreased to 12.09%, while the remaining groups showed areas of 50.08%, 41.09%, 27.02%, and 21.48% respectively (Fig. 6d) [1]. Figure 6c illustrates the trend of abscess wound area over ten days. Additionally, Figure S11 presents thermal imaging of mice treated with near-infrared irradiation, showing that the abscess site temperature in the VO_2 injection group reached 55.7 °C. Following ten days, excised skin tissue from the abscess site was ground and subjected to bacterial plate counting. Figure 6e indicates the lowest bacterial count in the VO2 + H2O2 + NIR group, with a survival rate of only 1.9% (Fig. 6f). These results demonstrate that the VO2-mediated PTT + CDT combination therapy effectively eradicates bacteria.

Pathological tissue evaluation of VO_2-mediated PTT + CDT

To investigate the therapeutic effects of VO_2 on the mouse skin further, we performed histological section staining and immunofluorescence analysis on the affected skin areas ten days post-infection. Hematoxylin and eosin (H&E) staining was used to assess the degree of inflammation in the infected skin tissue (Fig. 6g). The group of PBS-treated controls exhibited severe inflammatory cell infiltration, including abundant neutrophils and lymphocytes. In the group with VO2 + H_2O_2 + near-infrared light, inflammatory infiltration was significantly reduced. The remaining groups showed varying degrees of inflammatory cell infiltration. In addition, Masson's trichrome staining was used to visualize collagen fiber distribution [49], where collagen fibers appear blue-green and muscle fibers appear red (Fig. 6g). While the VO2 + H2O2 + NIR group exhibited the highest blue collagen content, the PBS group showed almost no blue collagen.

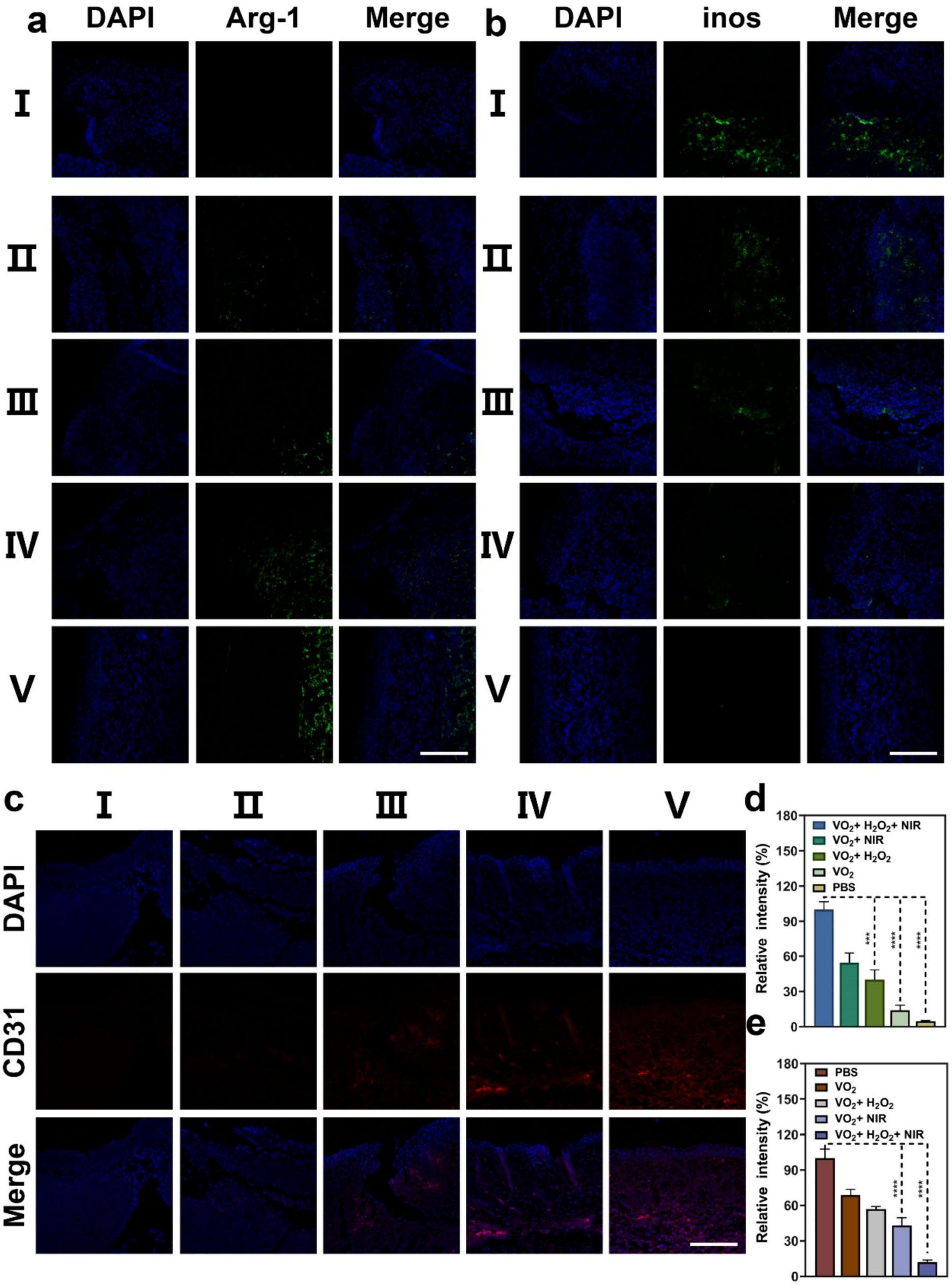

Fig. 7 (See legend on next page.)

(See figure on previous page.)

Fig. 7 Immunofluorescence analysis of subcutaneous abscess tissues in mice after different treatments. (**a**) Arg 1 immunofluorescence shows M2 macrophage accumulation. Scale bar, 200 μm. (**b**) iNOS immunofluorescence shows M1 macrophage accumulation. Scale bar, 200 μm. (**c**) Immunofluorescence staining results of CD31 on day 10. Scale bar, 200 μm. (**d**) Immunofluorescence quantification analysis derived from (**a**). (**e**) Immunofluorescence quantification analysis derived from (**b**). Ⅰ: PBS; Ⅱ: VO_2; Ⅲ: $VO_2+H_2O_2$; Ⅳ: VO_2+NIR; Ⅴ: $VO_2+H_2O_2+NIR$. Data are presented as mean ± SD ($n=3$), *$p<0.05$, **$p<0.01$, ***$p<0.001$, ****$p<0.0001$

Gram staining was used to monitor skin bacterial infection [50], with staining results serving as an indirect indicator of bacterial quantity (Fig. 6g). The PBS Group exhibited deep purple staining, indicating substantial Gram-positive bacterial infection, whereas the VO2 + H2O2 + NIR Group showed only minimal bacterial presence. These staining results confirm the significant antibacterial potential of the VO2 combined with PTT + CDT. During wound infection and healing, two macrophage types are typically involved: M1 and M2 macrophages [51]. M1 macrophages produce pro-inflammatory cytokines and reactive nitrogen species, participating in anti-infection and pro-inflammatory responses; whereas M2 macrophages secrete anti-inflammatory cytokines, primarily responsible for tissue repair and inflammation resolution. In skin tissue collected from the PBS group on day 10, the M1 macrophage marker (iNOS) exhibited significant fluorescent labeling, while the M2 marker (Arg 1) was nearly undetectable (Fig. 7a and b). The VO_2 group exhibited abundant iNOS fluorescence signals, which gradually diminished following near-infrared light and H_2O_2 treatment. Correspondingly, Arg 1 fluorescence intensity progressively increased. This finding indicates that skin in the PBS group remained in the anti-infective and pro-inflammatory phase, consistent with H&E staining results. Conversely, the VO2 + H_2O_2 + NIR group exhibited weak iNOS fluorescence and strong Arg 1 fluorescence, suggesting this group had progressed to the tissue repair phase. Quantitative fluorescence analysis of iNOS and Arg 1 further confirmed this conclusion (Fig. 7d and e). As a key indicator of the tissue repair phase, the angiogenesis marker CD31 holds significant importance. As shown in Fig. 7c, the VO2 + H_2O_2 group exhibited weak red fluorescence signals, while the VO2 + H_2O_2 + NIR group demonstrated the highest fluorescence intensity (Figure S12), indicating that combined VO2 therapy significantly promotes tissue repair and angiogenesis.

Conclusions

Overall, this work successfully synthesised M-phase VO_2 nanoparticles via a one-step hydrothermal method. Results indicate that V^{4+} sites on their surface are pivotal for generating enzyme-like activity. These nanoparticles, while retaining oxidase-like and peroxidase-like functions, can significantly enhance antimicrobial efficacy when combined with photothermal therapy. Furthermore, VO_2 exhibits notable anti-biofilm effects with negligible biotoxicity. Moreover, VO_2 modulates relevant macrophage markers in vivo, promotes skin healing in abscesses, and accelerates angiogenesis. In summary, we have developed a VO_2 nanoparticle system for combined therapy, which holds promise as a novel antimicrobial strategy against MDR bacterial infections. However, whilst this study focused on validating the superior efficacy of VO_2 nanoparticles in localised drug-resistant bacterial infection models, further exploration of their therapeutic potential in systemic infection models (e.g., bacteraemia) or organ-specific infection models (e.g., pneumonia) will be crucial for comprehensively evaluating the clinical translational value of this platform.

Supplementary Information

The online version contains supplementary material available at https://doi.org/10.1186/s12951-025-03799-9.

Supplementary Material 1.

Acknowledgements
The authors gratefully acknowledge the support from the Zhejiang Provincial Natural Science Foundation for Distinguished Young Scholars (LR23C100001).

Author contributions

Weicong Fu, Tian Huang and Yi-Xin Wang : Writing – original draft, Methodology, Data curation. Jing Zhao : Investigation, Methodology, Data curation. Jianliang Shen and Qining Yang : Writing – review & editing, Supervision, Funding acquisition.

Data availability

No datasets were generated or analysed during the current study.

Declarations

Competing interests

The authors declare no competing interests.

Author details
[1]Jinhua Municipal Central Hospital, Affiliated Jinhua Hospital, Zhejiang University School of Medicine, Jinhua 321000, China
[2]School of Pharmacy, Jiangxi Science & Technology Normal University, Nanchang 330013, Jiangxi, China
[3]School of Optometry and Vision Sciences, Cardiff University, Cardiff, UK
[4]Affiliated Hospital of Xiangnan University , Chenzhou, Hunan 423000, China
[5]National Engineering Research Center of Ophthalmology and Optometry, Eye Hospital, Wenzhou Medical University, Wenzhou 325027, China
[6]Wenzhou Institute, University of Chinese Academy of Sciences, Wenzhou 325000, China

Received: 25 July 2025 / Accepted: 17 October 2025

References

1. Jessy Mercy D, Thirumalai A, Udayakumar S, Deepika B, Janani G, Girigoswami A, et al. Enhancing wound healing with nanohydrogel-entrapped plant extracts and nanosilver: an in vitro investigation. Molecules. 2024;29(21):5004.
2. Mohammed SE, Hamid OM, Ali SS, Allam M, Elhussein AM. Prevalence of multidrug-resistant, extensively drug-resistant and pandrug-resistant *Pseudomonas aeruginosa* from clinical isolates in Khartoum State, Sudan. Am J Infect Dis Microbiol. 2023;11(1):1–7.
3. Adedeji-Olulana AF, Wacnik K, Lafage L, Pasquina-Lemonche L, Tinajero-Trejo M, Sutton JAF, et al. Two codependent routes lead to high-level MRSA. Science. 2024;386(6721):573–80.
4. Abdou Mohamed MA, Kozlowski HN, Kim J, Zagorovsky K, Kantor M, Feld JJ, et al. Diagnosing antibiotic resistance using nucleic acid enzymes and gold nanoparticles. ACS Nano. 2021;15(6):9379–90.
5. Dyzenhaus S, Sullivan MJ, Alburquerque B, Boff D, van de Guchte A, Chung M, Fulmer Y, Copin R, Ilmain JK, O'Keefe A, Altman DR, Stubbe F-X, Podkowik M, Dupper AC, Shopsin B, van Bakel H, Torres VJ. MRSA lineage USA300 isolated from bloodstream infections exhibit altered virulence regulation. Cell Host Microbe. 2023;31(2):228–e2428.
6. Li G, Feng Z, Hou Z, Chen R, Cui H, Wang T, Li P. Dual-Cascade Responsive H2Se Delivery Nanogels Bearing Selenobenzamide as H2Se Donor for the Treatment of Multidrug Resistant Bacteria Infections, Advanced Functional Materials n/a(n/a) 2418229.
7. Durgadevi P, Girigoswami K, Girigoswami A. Photophysical process of Hypocrellin-based photodynamic therapy: an efficient antimicrobial strategy for overcoming multidrug resistance. Physics. 2025;7(3):28.
8. Pallavi P, Harini K, Crowder S, Ghosh D, Gowtham P, Girigoswami K, et al. Rhodamine-conjugated anti-Stokes gold nanoparticles with higher ROS quantum yield as theranostic probe to arrest cancer and MDR bacteria. Appl Biochem Biotechnol. 2023;195(11):6979–93.
9. Zhang Y, Wei G, Liu W, Li T, Wang Y, Zhou M, et al. Nanozymes for nanohealthcare. Nat Rev Methods Primers. 2024;4(1):36.
10. Zhang L, Wang H, Qu X. Biosystem-inspired engineering of nanozymes for biomedical applications. Adv Mater. 2024;36(10):2211147.
11. Cao C, Yang N, Wang X, Shao J, Song X, Liang C, et al. Biomedicine meets nanozyme catalytic chemistry. Coord Chem Rev. 2023;491:215245.
12. Lin Z, Yuan J, Niu L, Zhang Y, Zhang X, Wang M, et al. Oxidase mimicking nanozyme: classification, catalytic mechanisms and sensing applications. Coord Chem Rev. 2024;520:216166.
13. Huang X, Zhang S, Tang Y, Zhang X, Bai Y, Pang H. Advances in metal–organic framework-based nanozymes and their applications. Coord Chem Rev. 2021;449:214216.
14. Feng Y, Coradi Tonon C, Ashraf S, Hasan T. Photodynamic and antibiotic therapy in combination against bacterial infections: efficacy, determinants, mechanisms, and future perspectives. Adv Drug Deliv Rev. 2021;177:113941.
15. Zhao Y, Zhao S, Du Y, Gao Z, Li Y, Ma H, Li H, Ren X, Fan Q, Wu D, Wei Q. Inverse Oxide/Alloy-Structured Nanozymes with NIR-Triggered Enzymatic Cascade Regulation of ROS Homeostasis for Efficient Wound Healing, Advanced Materials n/a(n/a) 2418731.
16. Zhao X, Chen Y, Niu R, Tang Y, Chen Y, Su H, et al. NIR plasmonic nanozymes: synergistic enhancement mechanism and multi-modal anti-infection applications of MXene/MOFs. Adv Mater. 2024;36(8):2307839.
17. Cao C, Zhang T, Yang N, Niu X, Zhou Z, Wang J, et al. POD nanozyme optimized by charge separation engineering for light/pH activated bacteria catalytic/photodynamic therapy. Signal Transduct Target Ther. 2022;7(1):86.
18. Liu J, Dong S, Gai S, Dong Y, Liu B, Zhao Z, et al. Design and mechanism insight of monodispersed AuCuPt alloy nanozyme with antitumor activity. ACS Nano. 2023;17(20):20402–23.
19. Wang W, Luo Q, Li L, Chen S, Wang Y, Du X, et al. Hybrid nickel-molybdenum bimetallic sulfide nanozymes for antibacterial and antibiofouling applications. Adv Compos Hybrid Mater. 2023;6(4):139.
20. Qi M-H, Wang D-D, Qian W, Zhang Z-L, Ao Y-W, Li J-M, et al. High-efficiency gold nanoaggregates for NIR LED-driven sustained mild photothermal therapy achieving complete tumor eradication and immune enhancement. Adv Mater. 2025;37(5):2412191.
21. Chang M, Hou Z, Wang M, Yang C, Wang R, Li F, et al. Single-atom Pd nanozyme for ferroptosis-boosted mild-temperature photothermal therapy. Angew Chem Int Ed. 2021;60(23):12971–9.
22. Wang P, Wang L, Zhan Y, Liu Y, Chen Z, Xu J, et al. Versatile hybrid nanoplatforms for treating periodontitis with chemical/photothermal therapy and reactive oxygen species scavenging. Chem Eng J. 2023;463:142293.
23. Dinda R, Garribba E, Sanna D, Crans DC, Costa Pessoa J. Hydrolysis, ligand exchange, and redox properties of vanadium compounds: implications of solution transformation on biological, therapeutic, and environmental applications. Chem Rev. 2025;125(3):1468–603.
24. Zhu H, Li T, Peng X, Zhang X, Zhang X, Wang Q, Lei L, Zhang J, He B, Cao J. Tumor Microenvironment-Driven Structural Transformation of Vanadium-Based MXenzymes to Amplify Oxidative Stress for Multimodal Tumor Therapy, Advanced Science n/a(n/a) 2408998.
25. Li K, Yang Y, Zhao J, Zhou Q, Li Y, Yang M, et al. Associations of metals and metal mixtures with glucose homeostasis: a combined bibliometric and epidemiological study. J Hazard Mater. 2024;470:134224.
26. Zhao R, Zhu Y, Feng L, Liu B, Hu Y, Zhu H, et al. Architecture of Vanadium-based MXene dysregulating tumor redox homeostasis for amplified nanozyme catalytic/photothermal therapy. Adv Mater. 2024;36(2):2307115.
27. Thompson KH, Orvig C. Coordination chemistry of vanadium in metallopharmaceutical candidate compounds. Coord Chem Rev. 2001;219–221:1033–1053.
28. Cheng Q, Chen Y, Zou D, Li Q, Shi X, Qin Q, et al. Targeting metabolic adaptation of colorectal cancer with Vanadium-doped nanosystem to enhance chemotherapy and immunotherapy. Adv Sci. 2025;12(7):2409329.
29. Zhao R, Feng L, Zhu Y, Yu C, Zyuzin MV, Gai S, Chen D, Zhang S, Zhu H, Yang P. A Precision Mo4VC4-Based Nanomedicine for Effective Cancer Elimination by Harnessing Senescence Induction and Immunogenic Response, Advanced Functional Materials n/a(n/a) 2420600.
30. Zhao R, Zhang R, Feng L, Dong Y, Zhou J, Qu S, et al. Constructing virus-like SiOx/CeO2/VOx nanozymes for 1064 nm light-triggered mild-temperature photothermal therapy and nanozyme catalytic therapy. Nanoscale. 2022;14(2):361–72.
31. Pan M, Zhong H, Wang S, Liu J, Li Z, Chen X, et al. Properties of VO2 thin film prepared with precursor VO(acac)2. J Cryst Growth. 2004;265(1):121–6.
32. Minić DM, Blagojević VA. Hydrothermal synthesis and controlled growth of vanadium oxide nanocrystals. CrystEngComm. 2013;15(33):6617–24.
33. Wang S, Owusu KA, Mai L, Ke Y, Zhou Y, Hu P, et al. Vanadium dioxide for energy conservation and energy storage applications: synthesis and performance improvement. Appl Energy. 2018;211:200–17.
34. Muñoz-Rojas D, Baudrin E. Synthesis and electroactivity of hydrated and monoclinic rutile-type nanosized VO2. Solid State Ionics. 2007;178(21):1268–73.
35. Karahan O, Tufani A, Unal S, Misirlioglu IB, Menceloglu YZ, Sendur K. Synthesis and morphological control of VO2 nanostructures via a one-step hydrothermal method. Nanomaterials. 2021;11(3):752.
36. Tang Y, Zhou X, Lei M, Wang H, Lu A, Zhang G, et al. Highly efficient catalytic debromination of tetrabromodiphenyl ether with hydrazine as reducing agent: the role of the interaction between the catalyst and the reducing agent. Chem Eng J. 2022;433:134364.
37. You Q, Jiang X-L, Fan W, Cui Y-S, Zhao Y, Zhuang S, et al. Pd8 nanocluster with nonmetal-to-metal- ring coordination and promising photothermal conversion efficiency. Angew Chem Int Ed. 2024;63(3):e202313491.
38. Zhang H, Ma J, Liu C, Li L, Xu C, Li Y, et al. Antibacterial activity of guanidinium-based ionic covalent organic framework anchoring Ag nanoparticles. J Hazard Mater. 2022;435:128965.
39. Thirumalai A, Sharmiladevi P, Girigoswami K, Prabhu AD, Girigoswami A. Tuneable carbon dots coated iron oxide nanoparticles as superior T (1) contrast agent for multimodal imaging. Admet Dmpk. 2025;13(3):2790.
40. Liu J, Yang D, Hu W, Huang N, Rong Y, Long Y, et al. Piezoelectric BaTiO3 nanoparticles as oxidase mimics breaking pH limitation for colorimetric detection of glutathione reductase. Chem Eng J. 2024;481:148609.
41. Liu H, Wei X, Peng H, Yang Y, Hu Z, Rao Y, Wang Z, Dou J, Huang X, Hu Q, Tan L, Wang Y, Chen J, Liu L, Yang Y, Wu J, Hu X, Lu S, Shang W, Rao X. LysSYL-Loaded pH-Switchable Self-Assembling peptide hydrogels promote Methicillin-Resistant Staphylococcus aureus elimination and wound healing. Adv Mater. 2024;36(52):e2412154.
42. Li N, Yan Y, Xia B-Y, Wang J-Y, Wang X. Novel tungsten carbide nanorods: an intrinsic peroxidase mimetic with high activity and stability in aqueous and organic solvents. Biosens Bioelectron. 2014;54:521–7.
43. Capdevila-Cortada M. It's a radical trap. Nat Catal. 2023;6(2):105–105.
44. Wu Z-L, Shih Y-J. Bimetallic palladium-tin nanoclusters, PdSn(200) and PdSn(101), templated with cationic surfactant for electrochemical denitrification toward N2 and NH4 + selectivity. Chem Eng J. 2022;433:133852.
45. Zhou J, Xu D, Tian G, He Q, Zhang X, Liao J, et al. Coordination-driven self-assembly strategy-activated Cu single-atom nanozymes for catalytic tumor-specific therapy. J Am Chem Soc. 2023;145(7):4279–93.

46. Wang J-L, Pan X, Li X, Liu K-M, Yao M, An J-Y, et al. Photoimmunologic therapy of stubborn biofilm via inhibiting bacteria revival and preventing reinfection. Adv Mater. 2025;37(6):2411468.
47. Zhuang P, Yang W, Zhang Y, Chen Y, Ding T, Chen Y, et al. In situ generating CO gas for destroying bacterial biofilms. Nano Today. 2024;56:102296.
48. Mei L, Zhu S, Liu Y, Yin W, Gu Z, Zhao Y. An overview of the use of nanozymes in antibacterial applications. Chem Eng J. 2021;418:129431.
49. Fan X, Hou J, Zi L, Chen W. Iron chelation therapy failed to improve cardiac dysfunction caused by mitochondrial injury in rats with iron overload cardiomyopathy a 7T cardiac MR research in vivo. Eur Heart J. 2024;45:ehae666.271. https://doi.org/10.1093/eurheartj/ehae666.271
50. Işıl Ç, Koydemir HC, Eryilmaz M, de Haan K, Pillar N, Mentesoglu K, et al. Virtual gram staining of label-free bacteria using dark-field microscopy and deep learning. Sci Adv. 2025;11(2):eads2757.
51. Chen S, Saeed AFUH, Liu Q, Jiang Q, Xu H, Xiao GG, et al. Macrophages in immunoregulation and therapeutics. Signal Transduct Target Ther. 2023;8(1):207.

Publisher's note